Enabling quantum optomechanics for phononic crystals and superfluid helium films

Wei, X.

Part II

Superfluid optomechanics

Chapter 5

Background on Superfluid Helium and Nonlinear Dynamics

5.1 Historical overview

In Part II of this thesis we present experimental results on nonlinear dynamics of a thin superfluid Helium film on top of an optical ring resonator. We have three long-term motivations for this research. The first is to explore the possibilities for creating macroscopic quantum superposition states of superfluid motion through interaction with light [32, 38], the second is to explore the intrinsic nonlinear motion of superfluid waves to implement well-defined multilevel quantum systems that could be explored in a similar fashion as superconducting circuits for quantum computation [37], and third, superfluid itself is of fundamental interest as a model system for quantum field theory with internal symmetry groups [61, 62].

We now give a brief overview of the discovery and investigations of superfluid Helium. There are two types of superfluid Helium, superfluid helium-4, a Bose-Einstein condensate, and superfluid helium-3, a condensate of paired helium-3 atoms in the paired triplet nuclear-spin state. We start with helium-4 which was discovered and explored first because of the relatively high superfluid transition temperature of $\sim 2.17\,\mathrm{K}$, compared to $\sim 2.7\,\mathrm{mK}$ for superfluid helium-3.

In 1908, the Dutch physicist Heike Kamerlingh Onnes achieved the first liquefaction of helium at Leiden University, reaching a temperature of 4.2 K. Performing experiments at such record-low temperatures led to the discovery of superconductivity in 1911 [63]. This groundbreaking work earned him the Nobel Prize in Physics in 1913 [64].

In 1938, the Soviet physicist Pyotr Leonidovich Kapitsa discovered that liquid helium exhibits zero viscosity below the λ point ($\sim 2.17\,\mathrm{K}$) [27]. In the same year, the British physicists John F. Allen and A. D. Misener independently observed similar phenomena. Their research demonstrated that liquid helium transitions into such a novel phase, characterized by frictionless flow, when cooled below 2.17 K [65].

In 1938, Fritz London published theoretical work that showed that the superfluid behavior of helium-4 could be explained by Bose–Einstein condensation. A significant fraction of helium-4 atoms condenses to the lowest quantum state below the λ point, leading to macroscopic quantum phenomena such as frictionless flow [66].

In 1939, Heinz London presented theoretical work predicting that a temperature gradient in a superfluid can cause a pressure difference that leads to fluid flow in a direction opposite to conventional expectations. The helium response to temperature gradients could not be explained using classical fluid dynamics, which provided strong evidence that the superfluid component could flow without viscosity, independent of the normal component's behavior. This theoretical framework supports the "two-fluid" model of helium [67].

In 1941, Lev Landau explained that the unique properties of liquid helium could be understood by considering its excitation spectrum, which includes two types of elementary excitations: phonons (quantized sound waves) and rotons (quantized vortex-like excitations). This concept led to the development of the two-fluid model, describing helium II as a mixture of a viscous normal component, made up of the excitations in the superfluid, and a pure superfluid component that experiences no viscous damping [28].

In 1949, Lev Landau further developed his theoretical framework for understanding superfluid helium. He proposed that the energy spectrum of these excitations is crucial for explaining the unique properties of superfluidity. Additionally, Landau introduced the concept of a critical velocity, suggesting that superfluid flow remains dissipationless below this threshold but becomes dissipative when the flow velocity exceeds it [68]. Up to today, this pragmatic model which describes superfluid helium-4 as a coexistence of two distinct components: a “normal” fluid and a “superfluid” component, is adopted to explain superfluid phenomena.

In 1956, Oliver Penrose and Lars Onsager introduced a generalized mathematical framework for Bose-Einstein condensation applicable to systems of interacting particles. They estimate that approximately 8% of helium atoms are in the condensed state, based on properties of the ground-state wave function and the assumption of no long-range configurational order at absolute zero temperature [69].

In 1965, P.C. Hohenberg and P.C. Martin presented an analysis of interacting condensed Bose systems, focusing on properties that are independent of the interaction potential's strength. This work is notable for its detailed examination of superfluid helium, providing insights into its microscopic behavior [70].

Later on, there appeared multiple theoretical works based on the wave functions to describe superfluid helium. Such as by P. W. Anderson, who introduced that the dissipative processes in superfluid flow are accompanied by phase slippage, offering insights into the mechanisms of energy loss in a superfluid system [71].

In 1964, G.W. Rayfield and F. Reif demonstrated that charged particles in superfluid helium at low temperatures could be accelerated to generate freely moving, charge-carrying vortex rings. This provided direct evidence of quantized vortices in superfluid helium. The study estimated the core radius of the vortex rings to be approximately 1 Ångström, providing insight into the microscopic structure of vortices in superfluid helium [72].

In 1995, the density functional for liquid helium that accurately accounts for the static response function and the phonon-roton dispersion relation in the uniform liquid was formulated [73].

In 2006, Gregory P. Bewley introduced a novel technique for directly imaging quantized vortex cores in superfluid helium by generating small solid hydrogen particles within liquid helium, which preferentially trapped along the cores of quantized vortices [74]. In 2014, Luis F. Gomez and his cooperators successfully visualized individual superfluid helium-4 nanodroplets containing approximately 10^8 to 10^{11} atoms by utilizing single-shot femtosecond x-ray coherent diffractive imaging [75].The earliest work of imaging vortex in superfluid was by E.J. Varmchuk and M.J.V. Gordon in 1979 [76].

A useful physical model is to consider that the vortex lines can dynamically reconnect [77]. The researchers achieved the first direct experimental visualization of reconnection events between quantized vortices in superfluid helium [78].

Another topic that has attracted considerable attention in the scientific community is helium-3. Compared to helium-4, helium-3 exhibits a much broader range of quantum phenomena, which has inspired a substantial body of theoretical research aimed at understanding its complex behavior. The reason why superfluid helium-3 is a much richer dynamical system than helium-4 (a simple condensate of bosonic atoms, with only one U(1) order parameter) is that it is a condensate of pairs of fermionic atoms in the spin-triplet state. Because the triplet nuclear spin state has SU(2) symmetry and is bosonic in nature, there must be a fermionic angular momentum part of the total wave function (in order to obey overall fermionic systemtry). This angular momentum part represents also a SU(2) symmetry. Together with the overall U(1) phase symmetry, there is a total of 7 order paramters (3 for each SU(2) symmetry and 1 for U(1)).

In 1972, David M. Lee, Douglas D. Osheroff and Robert C. Richardson observed the superfluidity in helium-3 below 2.7 mK [79]. They were awarded the Nobel Prize in Physics in 1996 [80].

In 1976, N. D. Mermin and Tin-Lun Ho introduced significant theoretical insights into the behavior of superfluid helium-3 in its A phase [81].

A broader overview of the theoretical and experimental developments in superfluid helium can be found in Refs. [82–84].

Because superfluid helium-3 requires temperatures below 2 mK, it is extremely challenging to perform experiments in this regime, especially experiments based on interactions with light, which results in increases in temperature due to photon absorption. In this thesis we will be exclusively dealing with helium-4 but future experiments with helium-3 are being planned. For this nuclear adiabatic demagnatization cooling is considered and available in our cryogenic system, to reach the required temperature range of around 1 mK.

Research on superfluid helium has a long history and has led to many important advances, yet a number of physically relevant questions remain open. Examples include quantum turbulence and vortex dynamics in He II, non-equilibrium thermodynamics and heat transport in confined geometries and thin films, as well as the interaction between superfluid helium and light. Because of these open problems, superfluid-helium physics has attracted increasing attention in recent years. The research presented in this thesis addressees these open questions in a unique system in which optical excitation and readout of the superfluid film dynamics is achieved.

In order to venture into this unexplored regime it is important to have a firm understanding of the theoretical methods that are commonly used in the study of superfluid Helium. Those methods are not derived from first principles but are based on a pragmatic modeling of experimental observations.

5.2 Phase diagram of He I / He II

Liquid helium exhibits a wide range of unique physical properties that make it an important subject of study in low-temperature physics. The phase transitions among its gaseous, liquid, and solid states are critically dependent on both temperature and pressure. Furthermore, under sufficiently low temperatures and appropriate pressure conditions, helium-4 enters a superfluid phase, which is an intrinsically quantum state characterized by the complete absence of viscosity and the emergence of macroscopic quantum coherence. This superfluid state provides a fundamental platform for the investigation of quantum mechanical effects at the macroscopic scale.

The phase diagram of helium-4, see Figure 5.1, exhibits several unique features due to its quantum mechanical nature and exceptionally weak interatomic forces [83]. At higher temperatures and pressures, helium exhibits a critical point at approximately 5.19 K and 2.29 MPa, beyond which the distinction between liquid and gas phases disappears. At atmospheric pressure, helium remains in the gaseous phase down to its boiling point at 4.22 K.

Upon further cooling at saturated vapor pressure, it transforms into a liquid phase which exists in two distinct states: normal liquid helium (Helium I) and superfluid helium (Helium II). The transition between Helium I and Helium II occurs along the so-called λ-line at approximately 2.17 K. Above this temperature the liquid helium behaves as a normal fluid which is known as helium I phase. In this regime, it exhibits classical fluid properties, for instance finite viscosity and thermal conductivity governed by standard diffusive processes. Below this temperature and at sufficiently low pressures, helium enters the Helium II phase, which is the superfluid phase characterized by zero viscosity and quantized vortices.

Furthermore, helium II exhibits exceptionally high thermal conductivity, which arises not from diffusive transport but from the propagation of entropy via second sound waves. The second sound wave is a unique mode of temperature wave propagation analogous to ordinary sound waves. Unlike any other element, helium does not solidify at ambient pressure even when cooled to absolute zero. Solidification of ^{4}He requires applying an external pressure of about 2.5 MPa or higher.

These unusual phase boundaries make liquid ^{4}He an ideal model system for studying quantum fluidity, Bose-Einstein condensation, and other low-temperature quantum phenomena. In particular, the existence of a stable liquid phase down to the lowest temperatures allows macroscopic quantum effects to play a central role in its flow properties. These effects are conveniently captured by the two-fluid model, which will

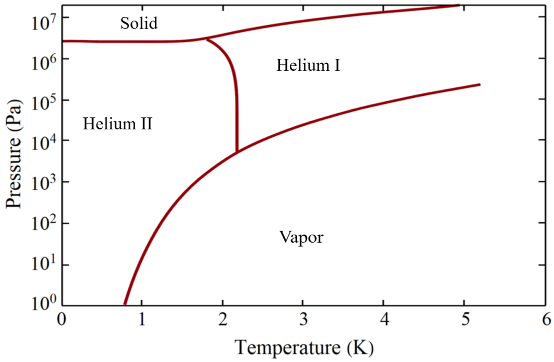

Figure 5.1: Phase diagram of helium-4 (adapted from Ref. [83]).

be introduced in the next section.

5.3 Two-fluid model

The theoretical understanding of superfluidity in helium-4 was facilitated by the development of the two-fluid model, initially proposed by László Tisza in 1938 [85] and later refined by Lev Landau [28, 68]. According to this model, liquid Helium II is treated as a mixture of two interpenetrating components: a normal fluid component that carries entropy and behaves like a classical liquid, and a superfluid component that is entropy-free and capable of frictionless flow. The total density ϱ of the system is the sum of the densities of these two components: $\varrho = \varrho_n + \varrho_s$, where ϱ_n and ϱ_s denote the densities of the normal and superfluid components. As the temperature approaches absolute zero, the normal component vanishes ($\varrho_n \to 0$) and the system becomes purely superfluid.

5

The momentum density $\boldsymbol{j}$, also referred to as the mass current density, of mass flow per unit volume is:

$$\boldsymbol{j} = \varrho_n \boldsymbol{v}_n + \varrho_s \boldsymbol{v}_s, \tag{5.1}$$

where $\mathbf{v}_n$ and $\mathbf{v}_s$ are the velocity of the normal and superfluid component, respectively. The mass conservation condition requires:

$$\frac{\partial \varrho}{\partial t} = -\operatorname{div} \boldsymbol{j}. \tag{5.2}$$

As mentioned before, the viscosity of the normal component is non-zero, but still very small below the lambda temperature. Therefore, in order to derive approximate equations of fluid motion it is reasonable to neglect the viscocity of the normal component. The superfluid helium can thus be treated as an ideal fluid. In this case, the momentum density obeys

$$\frac{\partial \boldsymbol{j}}{\partial t} + \underbrace{\varrho\, \boldsymbol{v} \cdot \operatorname{grad} v}_{\approx 0} = -\operatorname{grad} p \tag{5.3}$$

where p denotes the pressure and $\boldsymbol{v}$ the fluid velocity field. This is the fluid version of Newton's second law $\boldsymbol{F} = m\boldsymbol{a}$ written per unit volume. The x-component of Eq. 5.3 reads:

$$\frac{\partial j_x}{\partial t} + \varrho \left(v_x \frac{\partial v_x}{\partial x} + v_y \frac{\partial v_x}{\partial y} + v_z \frac{\partial v_x}{\partial z} \right) = -\frac{\partial p}{\partial x}. \tag{5.4}$$

The first term can be written as

$$\frac{\partial j_x}{\partial t} \simeq \varrho \frac{\partial v_x}{\partial t}. \tag{5.5}$$

Thus, the left hand side of Eq. 5.4 can be written as:

$$\varrho \left(\frac{\partial v_x}{\partial t} + v_x \frac{\partial v_x}{\partial x} + v_y \frac{\partial v_x}{\partial y} + v_z \frac{\partial v_x}{\partial z} \right) = \varrho \frac{d}{dt}\, v_x(x, y, z, t) \equiv \varrho \frac{D v_x}{Dt}. \tag{5.6}$$

The left-hand side of Eq. 5.4 is the total acceleration of a fluid parcel in the x direction multiplied by the mass density, describing how the fluid element is accelerated along the x direction. Eq. 5.3 can now be written compactly as

$$\varrho \frac{D\boldsymbol{v}}{Dt} = -\operatorname{grad} p. \tag{5.7}$$

Considering only small perturbations, where the velocity is small and the nonlinear convective term $\varrho\, \boldsymbol{v} \cdot \operatorname{grad} \boldsymbol{v}$ is of second order in $\boldsymbol{v}$. In a linear approximation it can therefore be neglected, and Eq. 5.3 reduces to

$$\frac{\partial \boldsymbol{j}}{\partial t} = -\operatorname{grad} p, \tag{5.8}$$

which shows that the change of mass current density is determined by the force density generated by the pressure gradient in this ideal regime.

Since the viscous friction is neglected and the superfluid helium carries no entropy, the total entropy of Helium II, modeled as a mixture of superfluid and normal components, is conserved in this approximation. Therefore the entropy is transported exclusively by the normal component, so the evolution of the entropy density involves only the normal components velocity $\mathbf{v}_n$:

$$\frac{\partial(\varrho S)}{\partial t} = -\operatorname{div}(\varrho S \mathbf{v}_n), \tag{5.9}$$

where S represents the entropy per unit mass and ϱS the entropy density.

We next analyze the dynamics of the normal and superfluid components. As a simple thought experiment, consider Helium II confined in a fixed volume V, and allow a small amount of entropy-free superfluid helium to be added. The resulting change in the internal energy is given by $dU = TdS - pdV + Gdm$, where G denotes the Gibbs free energy per unit mass at fixed temperature and pressure. It measures the total amount of useful (non-pV) work the system can deliver per unit mass under these conditions. In a single-component superfluid, G is identical to the chemical potential μ, which is the free-energy cost of adding one more particle (or, equivalently, per unit mass of the fluid) to the system at fixed temperature and pressure.

Under the approximation that no entropy is added ($dS = 0$) and no volume change occurs ($dV = 0$) while the mass changes by dm, the internal energy change reduces to $dU = G\,dm$. Thus, this idealized process affects only the mass of the superfluid component. The force per unit mass is then given by $f = -\operatorname{grad} G$. As a result:

$$\frac{d\mathbf{v}_s}{dt} = -\operatorname{grad}\mu, \tag{5.10}$$

which indicates that the acceleration of the superfluid component is driven by the gradient of the chemical potential.

5

The fundamental thermodynamic relation per unit mass is $d\varepsilon = TdS - pdV$, where ε is the specific internal energy, the internal energy per unit mass. The Gibbs free energy is defined as $G = \varepsilon + pV - TS$. Differentiating G gives $dG = d\varepsilon + pdV + Vdp - TdS - SdT$. Using the fundamental relation to eliminate $d\varepsilon$, this simplifies to $dG = -SdT + Vdp$. ((Here V denotes the specific volume, $V = V_{\text{tot}}/m = 1/\varrho$.)) Since $V = 1/\varrho$ and, for a single-component fluid, the specific Gibbs free energy equals the chemical potential ($G = \mu$), we finally obtain

$$\mathrm{d}\mu = -S\,\mathrm{d}T + \frac{1}{\varrho}\,\mathrm{d}p. \tag{5.11}$$

Since μ depends on T and p, its total differential has the general form for a function of two variables,

$$d\mu = \left(\frac{\partial\mu}{\partial T}\right)_p dT + \left(\frac{\partial\mu}{\partial p}\right)_T dp. \tag{5.12}$$

Comparing this expression with Eq. 5.11, we identify the partial derivatives as

$$\left(\frac{\partial \mu}{\partial T}\right)_p = -S, \qquad \left(\frac{\partial \mu}{\partial p}\right)_T = \frac{1}{\varrho}. \tag{5.13}$$

Viewing μ as a function of T and p, $\mu = \mu(T, p)$, the spatial chain rule for the gradient gives

$$\operatorname{grad}\mu = \left(\frac{\partial \mu}{\partial T}\right)_p \operatorname{grad}T + \left(\frac{\partial \mu}{\partial p}\right)_T \operatorname{grad}p. \tag{5.14}$$

Inserting these relations in Eq. 5.13 into Eq. 5.14 gives

$$\operatorname{grad}\mu = -S\operatorname{grad}T + \frac{1}{\varrho}\operatorname{grad}p. \tag{5.15}$$

Considering the linearized equation (Eq. 5.10) of motion for the superfluid component, we can obtain:

$$\frac{\partial \mathbf{v}_s}{\partial t} = S\operatorname{grad}T - \frac{1}{\varrho}\operatorname{grad}p, \tag{5.16}$$

which indicates that the superfluid components is driven along the temperature gradient towards the hotter region. In response to a pressure gradient, the superfluid component is accelerated from high to low pressure, as in an ordinary fluid.

To obtain the equation of motion for the normal component, we use total momentum conservation Eq. 5.1. In the absence of external forces and viscosity, the linearized momentum balance is Eq. 5.8. Assuming that ϱ_s and ϱ_n are time independent in the linearized regime, we obtain

$$\varrho_s\frac{\partial \mathbf{v}_s}{\partial t} + \varrho_n\frac{\partial \mathbf{v}_n}{\partial t} = -\operatorname{grad}p. \tag{5.17}$$

5

Using Eq. 5.16 for the superfluid acceleration, and substituting into Eq. 5.17, we find

$$\varrho_s\left(S\ \operatorname{grad}T - \frac{1}{\varrho}\ \operatorname{grad}p\right) + \varrho_n\frac{\partial \mathbf{v}_n}{\partial t} = -\operatorname{grad}p. \tag{5.18}$$

Rearranging terms and using $\varrho = \varrho_s + \varrho_n$, we can obtain:

$$\frac{\partial \mathbf{v}_n}{\partial t} = -\frac{\varrho_s}{\varrho_n}S\ \operatorname{grad}T - \frac{1}{\varrho}\ \operatorname{grad}p. \tag{5.19}$$

The normal component is accelerated toward the colder region in the presence of a temperature gradient, which is the opposite direction to the superfluid flow, realizing the characteristic thermal counterflow of Helium II. Under a pressure gradient, the normal component is accelerated from high to low pressure, just as in an ordinary fluid and the superfluid components.

While the two-fluid model provides a phenomenological description of these transport properties, the underlying origin of superfluidity is inherently quantum mechanical. Below the λ transition at $T_\lambda \approx 2.17$ K, liquid helium-4 enters a superfluid phase that exhibits macroscopic quantum coherence, a feature commonly associated with Bose–Einstein condensation (BEC). Unlike ideal Bose gases, where condensation occurs in the absence of interactions, the transition in helium-4 takes place within a strongly interacting system. These strong interatomic interactions make a simple mean-field description of BEC inadequate and require more complex treatments to capture the emerging collective phenomena.

Despite the complexity introduced by interactions, the superfluid phase of liquid helium-4 still exhibits essential features that are commonly associated with BEC. In this regime, the observed dissipation is extremely small and cannot be understood within a picture of classical friction alone. Instead, the stability of the superflow is a consequence of the quantum statistics and excitation spectrum of the interacting bosonic system. A macroscopic fraction of the particles occupies the same quantum state, and the excitation spectrum strongly limits scattering into low-energy excitations.

The first experimental evidence of superfluidity in liquid helium-4 was reported independently by Kapitza [27] and by Allen and Misener [65], marking an important milestone in low-temperature physics. A more formal description of this macroscopically coherent state is obtained by introducing a complex macroscopic wave function for the superfluid component,

$$\psi(\mathbf{r}) = \psi_0(\mathbf{r})e^{i\varphi(\mathbf{r})}, \tag{5.20}$$

where $\varphi(\mathbf{r})$ is the phase and the amplitude $\psi_0(\mathbf{r})$ is related to the local superfluid density via $\psi_0(\mathbf{r}) = \sqrt{\varrho_s(\mathbf{r})}$. Here $\varrho_s(\mathbf{r})$ denotes the number density of ^{4}He atoms in the superfluid component per unit volume. Within this description, the superfluid velocity is given by the gradient of the phase,

$$\mathbf{v}_s(\mathbf{r}) = \frac{\hbar}{m_4}\,\mathrm{grad}\,\varphi(\mathbf{r}), \tag{5.21}$$

with m_4 the mass of a ^{4}He atom. Since the velocity field is derived from a gradient, it is irrotational, $\nabla \times \mathbf{v}_s = 0$, in any simply connected region where the phase is single valued. This precludes classical rigid-body rotation and implies that circulation can only appear through singular vortex cores, around which the phase becomes multi-valued and the circulation is quantized in units of h/m_4.

The effectively vanishing viscosity observed in superfluid helium-4 thus exemplifies the macroscopic consequences of Bose statistics and quantum coherence in a strongly interacting system. Dissipative mechanisms that are common in classical fluids are strongly suppressed, not because collisions or interactions are absent, but because the quantum nature of the condensate and the structure of the excitation spectrum greatly reduce the phase space available for scattering processes.

These general considerations about superfluid transport provide the basis for understanding thermomechanical effects such as the fountain effect, where temperature gradients and counterflow give rise to pressure differences in Helium II.

5.4 Thermomechanical effects: the fountain effect

One of the most striking manifestations of superfluid transport in Helium II is the fountain effect, in which a temperature difference generates a pressure difference and causes the liquid to rise and even form a fountain. A schematic setup is shown in Figure 5.2, where a narrow-necked vessel is immersed in a bath of Helium II and connected to the surrounding liquid through a fine compressed powder layer, often referred as superleak, at its bottom. The superleak transmits the superfluid component, while the normal component is blocked from passing through it. Due to its fine internal structure, the superleak effectively provides a very large surface area. The viscous normal component then experiences very strong friction and its flow through the powder is negligible, whereas the superfluid component can still move through it. For the purpose of the experiment, the compressed powder is therefore idealized as a superleak that transmits only the superfluid component.

An electrical heater is placed just above the powder inside the flask to raise the temperature of the helium inside the bottle above the bath temperature. In the absence of heating, the helium in the bottle is in equilibrium with the surrounding bath. The liquid level inside rises until it matches the level of the bath, and the temperature and pressure are the same on both sides of the superleak.

When the heater is switched on, it raises the temperature of the helium in the bottle to $T_{\text{in}} > T_0$, while the bath remains at T_0. In the two-fluid picture, entropy is carried by the normal component, whereas the superfluid component has essentially zero entropy. When the heater is switched on, two main effect can occur: the first one

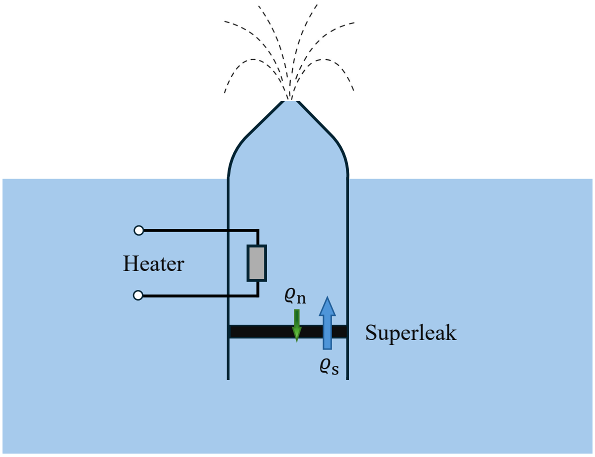

Figure 5.2: Schematic illustration of the fountain effect in superfluid helium. A narrow-necked vessel is immersed in a bath of He II and connected to it through a superleak that transmits only the superfluid component, while the normal component is effectively blocked. A heater inside the vessel locally raises the temperature of the surrounding bath, thereby establishing a temperature difference across the superleak. In response, superfluid flows through the superleak from the colder bath into the warmer interior of the vessel, leading to a buildup of pressure. This pressure increase causes the liquid to rise and, under steady heating, to sustain a stable fountain at the outlet.

is counterflow of superfluid and normal fluid components as will be described in the following paragraphs, the second effect is that the temperature increase generates excitations (phonons and quantized vortices), effectively converting part of the superfluid density into normal-fluid density and increasing the local entropy.

In the traditional fountain effect, typically demonstrated at sufficient high temperatures (of the order of 1 K) such that both the normal and superfluid densities are significant, the counterflow is the dominate effect. As we will see in Section 6.1, our experiments are performed at around 20 mK where the normal-fluid density is almost zero. Therefore the creation of the normal component by the heating plays an important role.

In the two-fluid description, the response of the two components to a temperature gradient is governed by Eqs. 5.16 and 5.19. Neglecting pressure gradients at early times, Eq. 5.16 shows that the superfluid component is accelerated in the direction of grad T, which is toward the hotter region, whereas Eq. 5.19 shows that the normal component is accelerated in the opposite direction. This is the origin of the thermal counterflow.

In steady state, the superfluid component is in diffusive equilibrium across the superleak, so the chemical potential must be equal on both sides of the superleak. This implies $\mathrm{d}\mu = 0$. For small changes in temperature and pressure, the chemical potential satisfies Eq.5.11: $\mathrm{d}\mu = -S\,\mathrm{d}T + v\,\mathrm{d}p$. Which gives

$$0 = -S\,\Delta T + v\,\Delta p \quad \Rightarrow \quad \Delta p = \frac{S}{v}\,\Delta T,$$

with $\Delta T = T_{\text{in}} - T_0 > 0$, so that the pressure inside the bottle increases to $p_{\text{in}} = p_0 + \Delta p$. This pressure rise is produced by superfluid flowing through the superleak into the warmer bottle until the chemical potentials on both sides match again.

As superfluid continues to flow in, the liquid level in the flask rises above the level of the bath. The excess pressure raises the liquid level in the neck and pushes helium out through the opening, producing a continuous fountain of helium emerging from the top of the bottle. As long as the heater maintains a temperature difference, the corresponding pressure difference persists and a steady fountain can be sustained.

Within the two-fluid description, this thermomechanical effect can be understood in terms of the chemical potential and the condition of mechanical and diffusive equilibrium between the two reservoirs. Small changes in temperature and pressure are related by Eq.5.11. In steady state the chemical potential must be equal on both sides of the superleak, $\mathrm{d}\mu = 0$, so that a temperature increase $\mathrm{d}T > 0$ on the heated side must be balanced by an increase in pressure $\mathrm{d}p > 0$.

5.5 First, second and third sound waves in He II

The fountain effect discussed above is a static manifestation of the thermomechanical properties of Helium II: a temperature difference across a superleak leads to a pressure difference and a steady flow. In the two-fluid picture, similar thermodynamic couplings also govern the dynamical response of the system. When the superfluid and normal components are subjected to small time-dependent perturbations, the coupled equations of motion support several distinct sound modes.

In bulk Helium II, there are two primary sound modes. First sound corresponds essentially to an ordinary pressure (density) wave in which the superfluid and normal components move in phase. Second sound, by contrast, is an entropy (temperature) wave in which the two components oscillate largely out of phase, giving rise to propagating temperature oscillations with only a small density change. In addition, when

He II forms a thin film on a substrate, a third mode can appear, characterized by oscillations of the film thickness driven by the superfluid component. In the following, we briefly summarize the physical origin and basic properties of first, second, and third sound in the framework of the two-fluid model.

In the two-fluid model of Helium II we use the linearized hydrodynamic equations, neglecting viscosity and external forces and restricting ourselves to small velocities and small departures from equilibrium.

Using Eqs. 5.1 and 5.9, we obtain

$$\frac{\partial \varrho}{\partial t} + \operatorname{div}\big(\varrho_s \boldsymbol{v}_s + \varrho_n \boldsymbol{v}_n\big) = 0. \tag{5.22}$$

Here $\varrho = \varrho_s + \varrho_n$ is the total mass density. In the linear regime, and neglecting convective and viscous terms, the equation of motion for the total momentum density is given by Eq. 5.8.

We use $\nabla\cdot\boldsymbol{A}$ and ∇f to denote the divergence of a vector field $\boldsymbol{A}$ and the gradient of a scalar field f, respectively, and write $\nabla^2 f = \nabla\cdot\nabla f$ for the Laplacian. Differentiating the continuity Eq.5.9: $\frac{\partial \varrho}{\partial t} = -\operatorname{div}\boldsymbol{j} = -\nabla\cdot\boldsymbol{j}$ with respect to time we obtain

$$\frac{\partial^2 \varrho}{\partial t^2} + \nabla\cdot\frac{\partial \boldsymbol{j}}{\partial t} = 0. \tag{5.23}$$

Using the equation of motion Eq. 5.8 to eliminate $\partial\boldsymbol{j}/\partial t$, Eq. 5.23 becomes

$$\frac{\partial^2 \varrho}{\partial t^2} = \nabla\cdot\nabla p, \tag{5.24}$$

5

This equation relates the second time derivative of the density to spatial variations of the pressure and provides the basic dynamical relation for density fluctuations in liquid helium.

From the experiments, the velocity of the two components are difficult to measure and therefore not preferred parameters in the theory. From Eq. 5.9, where S denotes the entropy per unit mass and hence ϱS is the entropy density, the entropy continuity equation reads

$$\frac{\partial(\varrho S)}{\partial t} + \nabla\cdot(\varrho S\,\boldsymbol{v}_n) = 0.$$

Moreover, the equation of motion for the superfluid velocity is given by Eq. 5.16,

$$\frac{\partial \boldsymbol{v}_s}{\partial t} = S\,\nabla T - \frac{1}{\varrho}\,\nabla p.$$

We can eliminate the normal velocity $\boldsymbol{v}_n$ and superfluid velocity $\boldsymbol{v}_s$ to obtain the equation for the entropy fluctuations.

Small deviations from a homogeneous equilibrium state are considered within the linear regime, so that $S = S_0 + \delta S$, where S_0 denotes the constant equilibrium value and δS the small deviation from equilibrium. This means $\frac{\partial S_0}{\partial t} = 0, \nabla S_0 = \mathbf{0}$. Inserting $S = S_0 + \delta S$ into Eq. 5.9 yields

$$\begin{aligned} 0 &= \frac{\partial}{\partial t}(S_0 + \delta S) + \nabla \cdot \big[(S_0 + \delta S)\, \boldsymbol{v}_n\big] \\ &= \frac{\partial S_0}{\partial t} + \frac{\partial \delta S}{\partial t} + \nabla \cdot \big(S_0 \boldsymbol{v}_n\big) + \nabla \cdot \big(\delta S\, \boldsymbol{v}_n\big) \\ &= \frac{\partial \delta S}{\partial t} + S_0\, \nabla \cdot \boldsymbol{v}_n + \nabla \cdot \big(\delta S\, \boldsymbol{v}_n\big), \end{aligned} \tag{5.25}$$

where S_0 is constant in space and time, so that $\partial_t S_0 = 0$ and $\nabla \cdot (S_0 \boldsymbol{v}_n) = S_0\, \nabla \cdot \boldsymbol{v}_n$.

In the linear regime, both δS and $\boldsymbol{v}_n$ are treated as first-order small quantities. The term $\nabla \cdot \big(\delta S\, \boldsymbol{v}_n\big)$ is therefore of second order in the fluctuations and is neglected. Keeping only terms up to first order, the entropy continuity equation reduces to

$$\frac{\partial \delta S}{\partial t} + S_0\, \nabla \cdot \boldsymbol{v}_n = 0. \tag{5.26}$$

Differentiating this equation once more with respect to time yields

$$\frac{\partial^2 \delta S}{\partial t^2} + S_0\, \nabla \cdot \frac{\partial \boldsymbol{v}_n}{\partial t} = 0. \tag{5.27}$$

To proceed we need an expression for $\partial \boldsymbol{v}_n / \partial t$. In the two-fluid model the total mass-current density is given by Eq. 5.1, and the linearized equation of motion for the total momentum density by Eq. 5.8,

$$\frac{\partial \boldsymbol{j}}{\partial t} + \nabla p = 0.$$

In the linear regime we may replace ϱ_s and ϱ_n by their equilibrium values, so that Eq. 5.8 becomes

$$\varrho_s \frac{\partial \boldsymbol{v}_s}{\partial t} + \varrho_n \frac{\partial \boldsymbol{v}_n}{\partial t} + \nabla p = 0. \tag{5.28}$$

Solving Eq. 5.28 for $\partial \boldsymbol{v}_n / \partial t$ gives

$$\varrho_n \frac{\partial \boldsymbol{v}_n}{\partial t} = -\nabla p - \varrho_s \frac{\partial \boldsymbol{v}_s}{\partial t}. \tag{5.29}$$

Next we insert the equation of motion for the superfluid velocity Eq. 5.16, into

5

Eq. 5.29. In the linear approximation we may replace S and ϱ by their equilibrium values S_0 and ϱ_0, so that Eq. 5.16 reduces to

$$\frac{\partial \boldsymbol{v}_s}{\partial t} \simeq S_0 \nabla T - \frac{1}{\varrho_0} \nabla p. \tag{5.30}$$

Substituting Eq. 5.30 into Eq. 5.29 we obtain

$$\begin{aligned} \varrho_n \frac{\partial \boldsymbol{v}_n}{\partial t} &= -\nabla p - \varrho_s \left(S_0 \nabla T - \frac{1}{\varrho_0} \nabla p \right) \\ &= -\nabla p - \varrho_s S_0 \nabla T + \frac{\varrho_s}{\varrho_0} \nabla p \\ &= -\left(1 - \frac{\varrho_s}{\varrho_0}\right) \nabla p - \varrho_s S_0 \nabla T \\ &= -\frac{\varrho_n}{\varrho_0} \nabla p - \varrho_s S_0 \nabla T, \end{aligned} \tag{5.31}$$

or

$$\frac{\partial \boldsymbol{v}_n}{\partial t} = -\frac{1}{\varrho_0} \nabla p - \frac{\varrho_s}{\varrho_n} S_0 \nabla T. \tag{5.32}$$

Inserting Eq. 5.32 into Eq. 5.27, and using the fact that all prefactors are spatially uniform in the linearized theory, we find

$$\begin{aligned} \frac{\partial^2 \delta S}{\partial t^2} &= -S_0 \nabla \cdot \frac{\partial \boldsymbol{v}_n}{\partial t} \\ &= -S_0 \nabla \cdot \left[-\frac{1}{\varrho_0} \nabla p - \frac{\varrho_s}{\varrho_n} S_0 \nabla T \right] \\ &= S_0 \frac{1}{\varrho_0} \nabla^2 p + S_0 \frac{\varrho_s}{\varrho_n} S_0 \nabla^2 T \\ &= \frac{S_0}{\varrho_0} \nabla^2 p + \frac{\varrho_s}{\varrho_n} S_0^2 \nabla^2 T. \end{aligned} \tag{5.33}$$

5

Equation 5.33 is the general linearized wave equation for the entropy (per unit mass), obtained by eliminating the velocities $\boldsymbol{v}_s$ and $\boldsymbol{v}_n$.

In many situations of interest the second term, proportional to $\nabla^2 T$, dominates the dynamics of the entropy fluctuations, while the contribution from $\nabla^2 p$ can be neglected. As usual in the linearized theory, we denote the entropy fluctuation again by S and write

$$\frac{\partial^2 S}{\partial t^2} = \frac{\varrho_s}{\varrho_n} S^2 \nabla^2 T. \tag{5.34}$$

Using Eqs. 5.24 and 5.34, the propagation of small density and entropy perturbations in

Helium II can be discussed within the above approximations. The four thermodynamic variables (ϱ, S, p, T) are not independent. In the following, the mass density ϱ and the entropy per unit mass S are chosen as independent variables. The pressure and temperature are then treated as state functions of these variables, $p = p(\varrho, S)$ and $T = T(\varrho, S)$, so that heir small variations can be written as

$$\delta p = \left(\frac{\partial p}{\partial \varrho}\right)_S \delta\varrho + \left(\frac{\partial p}{\partial S}\right)_\varrho \delta S, \tag{5.35}$$

$$\delta T = \left(\frac{\partial T}{\partial \varrho}\right)_S \delta\varrho + \left(\frac{\partial T}{\partial S}\right)_\varrho \delta S. \tag{5.36}$$

For small perturbations about a homogeneous equilibrium state the thermodynamic derivatives can be regarded as spatially constant. Applying the Laplacian to Eqs. 5.35 and 5.36, and noting that the equilibrium parts are spatially uniform, we obtain

$$\nabla^2 p = \left(\frac{\partial p}{\partial \varrho}\right)_S \nabla^2\varrho + \left(\frac{\partial p}{\partial S}\right)_\varrho \nabla^2 S, \tag{5.37}$$

$$\nabla^2 T = \left(\frac{\partial T}{\partial \varrho}\right)_S \nabla^2\varrho + \left(\frac{\partial T}{\partial S}\right)_\varrho \nabla^2 S. \tag{5.38}$$

Inserting Eq. 5.37 into the density equation Eq. 5.24 and Eq. 5.38 into the entropy equation 5.34 yields the coupled wave equations

$$\frac{\partial^2 \varrho}{\partial t^2} = \left(\frac{\partial p}{\partial \varrho}\right)_S \nabla^2\varrho + \left(\frac{\partial p}{\partial S}\right)_\varrho \nabla^2 S, \tag{5.39}$$

$$\frac{\partial^2 S}{\partial t^2} = \frac{\varrho_s}{\varrho_n} S^2 \left[\left(\frac{\partial T}{\partial \varrho}\right)_S \nabla^2\varrho + \left(\frac{\partial T}{\partial S}\right)_\varrho \nabla^2 S\right]. \tag{5.40}$$

5

These two equations are coupled wave equations for the density and entropy fluctuations. A standard approach to solving such equations is to use plane waves as an ansatz. We consider perturbations propagating along the x-axis and write

$$\varrho = \varrho_0 + \varrho'\, e^{i\omega(t-x/v)}, \qquad S = S_0 + S'\, e^{i\omega(t-x/v)}, \tag{5.41}$$

where ϱ' and S' denote the (complex) amplitudes, ω is the angular frequency and v the phase velocity of the wave propagating in the x-direction. Inserting these ansatz into Eq. 5.39, we can write the left side as

$$\begin{aligned}\frac{\partial^2 \varrho}{\partial t^2} &= \frac{\partial^2}{\partial t^2}\left[\varrho_0 + \varrho' e^{i\omega(t-x/v)}\right] \\ &= \varrho' \frac{\partial^2}{\partial t^2} e^{i\omega(t-x/v)} \\ &= \varrho'(i\omega)^2 e^{i\omega(t-x/v)} = -\omega^2 \varrho' e^{i\omega(t-x/v)}.\end{aligned} \tag{5.42}$$

$$\begin{aligned}\frac{\partial^2 S}{\partial t^2} &= \frac{\partial^2}{\partial t^2}\left[S_0 + S' \, e^{i\omega(t-x/v)}\right] \\ &= S' \frac{\partial^2}{\partial t^2} e^{i\omega(t-x/v)} \\ &= S'(i\omega)^2 e^{i\omega(t-x/v)} = -\omega^2 S' e^{i\omega(t-x/v)}.\end{aligned} \tag{5.43}$$

Similarly, the second spatial derivatives are

$$\nabla^2 \varrho = \frac{\partial^2 \varrho}{\partial x^2} = -\frac{\omega^2}{v^2}\, \varrho' e^{i\omega(t-x/v)}, \tag{5.44}$$

$$\nabla^2 S = \frac{\partial^2 S}{\partial x^2} = -\frac{\omega^2}{v^2}\, S' e^{i\omega(t-x/v)}. \tag{5.45}$$

Substituting these expressions into Eq. 5.39,

$$\frac{\partial^2 \varrho}{\partial t^2} = \left(\frac{\partial p}{\partial \varrho}\right)_S \frac{\partial^2 \varrho}{\partial x^2} + \left(\frac{\partial p}{\partial S}\right)_\varrho \frac{\partial^2 S}{\partial x^2}, \tag{5.46}$$

5

$$\begin{aligned}-\omega^2 \varrho' e^{i\omega(t-x/v)} &= \left(\frac{\partial p}{\partial \varrho}\right)_S \left[-\frac{\omega^2}{v^2}\, \varrho' e^{i\omega(t-x/v)}\right] + \left(\frac{\partial p}{\partial S}\right)_\varrho \left[-\frac{\omega^2}{v^2}\, S' e^{i\omega(t-x/v)}\right] \\ &= -\frac{\omega^2}{v^2}\, e^{i\omega(t-x/v)} \left[\left(\frac{\partial p}{\partial \varrho}\right)_S \varrho' + \left(\frac{\partial p}{\partial S}\right)_\varrho S'\right].\end{aligned} \tag{5.47}$$

Canceling the common factor $-\omega^2 e^{i\omega(t-x/v)}$ on both sides, we arrive at

$$v^2 \varrho' = \left(\frac{\partial p}{\partial \varrho}\right)_S \varrho' + \left(\frac{\partial p}{\partial S}\right)_\varrho S', \tag{5.48}$$

We now define the characteristic velocity

$$v_1^2 = \left(\frac{\partial p}{\partial \varrho}\right)_S, \tag{5.49}$$

so that Eq. 5.48 can be written as

$$(v^2 - v_1^2)\,\varrho' = \left(\frac{\partial p}{\partial S}\right)_\varrho S'. \tag{5.50}$$

Dividing by v_1^2 and using $(\partial\varrho/\partial p)_S = 1/(\partial p/\partial\varrho)_S = 1/v_1^2$, we obtain

$$\left[\left(\frac{v}{v_1}\right)^2 - 1\right]\varrho' - \left(\frac{\partial p}{\partial S}\right)_\varrho \left(\frac{\partial \varrho}{\partial p}\right)_S S' = 0. \tag{5.51}$$

Proceeding in the same way with Eq. 5.40, insertion of the plane-wave ansatz 5.41 gives

$$\begin{aligned} -\omega^2 S' e^{i\omega(t-x/v)} &= \frac{\varrho_s}{\varrho_n}\, S_0^2 \left[\left(\frac{\partial T}{\partial \varrho}\right)_S \left(-\frac{\omega^2}{v^2}\,\varrho' e^{i\omega(t-x/v)}\right) + \left(\frac{\partial T}{\partial S}\right)_\varrho \left(-\frac{\omega^2}{v^2}\, S' e^{i\omega(t-x/v)}\right)\right] \\ &= -\frac{\omega^2}{v^2}\, e^{i\omega(t-x/v)}\, \frac{\varrho_s}{\varrho_n}\, S_0^2 \left[\left(\frac{\partial T}{\partial \varrho}\right)_S \varrho' + \left(\frac{\partial T}{\partial S}\right)_\varrho S'\right]. \end{aligned} \tag{5.52}$$

Canceling the common factor $-\omega^2 e^{i\omega(t-x/v)}$ on both side, we get

$$S' = \frac{\varrho_s}{\varrho_n}\,\frac{S_0^2}{v^2} \left[\left(\frac{\partial T}{\partial \varrho}\right)_S \varrho' + \left(\frac{\partial T}{\partial S}\right)_\varrho S'\right]. \tag{5.53}$$

Multiplying by v^2 we obtain

$$v^2 S' = \frac{\varrho_s}{\varrho_n}\, S_0^2 \left[\left(\frac{\partial T}{\partial \varrho}\right)_S \varrho' + \left(\frac{\partial T}{\partial S}\right)_\varrho S'\right]. \tag{5.54}$$

We now introduce the second characteristic velocity

$$v_2^2 = \frac{\varrho_s}{\varrho_n}\, S_0^2 \left(\frac{\partial T}{\partial S}\right)_\varrho, \tag{5.55}$$

so that Eq. 5.54 can be written as

$$v^2 S' = \frac{\varrho_s}{\varrho_n} S_0^2 \left(\frac{\partial T}{\partial \varrho}\right)_S \varrho' + v_2^2 S'. \tag{5.56}$$

Rearranging terms we find

$$\left(v^2 - v_2^2\right) S' = \frac{\varrho_s}{\varrho_n} S_0^2 \left(\frac{\partial T}{\partial \varrho}\right)_S \varrho'. \tag{5.57}$$

Dividing by v_2^2 and using

$$\frac{1}{v_2^2} = \frac{\varrho_n}{\varrho_s} \frac{1}{S_0^2} \left(\frac{\partial S}{\partial T}\right)_\varrho,$$

we obtain

$$\left[\left(\frac{v}{v_2}\right)^2 - 1\right] S' - \left(\frac{\partial T}{\partial \varrho}\right)_S \left(\frac{\partial S}{\partial T}\right)_\varrho \varrho' = 0. \tag{5.58}$$

Equations 5.51 and 5.58 form a linear system for the amplitudes ϱ' and S' and constitute the general dispersion relations for sound propagation in Helium II within the two-fluid model. *Note that the sign of the second term differs from that given in the literature [86]. Here, the minus sign follows from the transformation between $T(S, \varrho)$ and $S(T, \varrho)$.*

The dynamical behavior of these two components gives rise to several distinct modes of generalized sound propagation in Helium II. The first sound corresponds to an ordinary pressure-density wave, in which both the normal and superfluid components oscillate in phase. In contrast, the second sound is a temperature-entropy wave, characterized by an out-of-phase oscillation of the two components, effectively a counterflow between the superfluid and normal fluid. This unique phenomenon is a direct consequence of the two-fluid formalism.

Unlike the first and second sound, third sound is a surface wave on a thin film. The normal component adheres to the surface through viscous forces while the superfluid components makes surfaces waves due to the van der Waals restoring forces and surface tensions. For more familiar surface water waves, the restoring force is gravity. Since third sound only partially influenced by gravity, it can flow along walls and ceilings because van der Waals forces.

5.5.1 First sound

For perturbations with a finite density fluctuation $\varrho' \neq 0$ and vanishing entropy fluctuation $S' = 0$, Helium II supports a sound mode that is very similar to an ordinary acoustic wave in a normal liquid. In this first-sound mode the two partial densities fluctuate in phase, so that the superfluid fraction remains constant, e.g. $\varrho_s'/\varrho_s = \varrho_n'/\varrho_n$.

Under these conditions temperature fluctuations are essentially absent and we can neglect temperature gradients, $\operatorname{grad} T \approx 0$. The resulting mode is an essentially adiabatic oscillation of pressure and total mass density, rather than a motion driven by temperature gradients.

Within the approximation $\operatorname{grad} T \approx 0$, substituting this condition back into the two–fluid equations Eq.5.8 and Eq.5.16 yields the important relation

$$\rho_n \frac{\partial}{\partial t}\big(\mathbf{v}_n - \mathbf{v}_s\big) = S \operatorname{grad} T = 0. \tag{5.59}$$

Since the right-hand side $S \operatorname{grad} T$ vanishes (because $\operatorname{grad} T \approx 0$), the left-hand side must also be zero. For time dependent oscillatory perturbations this implies

$$\mathbf{v}_n - \mathbf{v}_s = 0 \quad \Rightarrow \quad \mathbf{v}_n = \mathbf{v}_s. \tag{5.60}$$

Thus, in first sound the normal and superfluid components have identical velocities everywhere and move strictly in phase, so that no temperature gradient driven counterflow can be established.

Because $\mathbf{v}_n = \mathbf{v}_s$, the velocities of the two components are completely synchronized in space and time, i.e. they move strictly in phase. In other words, the normal and superfluid components have identical velocities everywhere and therefore move completely "locked" together. As a consequence, the total density undergoes adiabatic oscillations, while no temperature-gradient–driven counterflow is established. In this regime, He II behaves, as far as this sound mode is concerned, essentially like an ordinary liquid: one recovers the usual acoustic mode with propagation speed $v = v_1$.

In the low-temperature limit $T \to 0$, one finds that the first-sound velocity is approximately $v_1 \approx 238$ m/s. This estimate is obtained in the limit where the coupling between first and second sound can be neglected, so that the two modes do not mix or influence each other. In reality, as one approaches the λ point (the superfluid transition), the two modes become coupled, leading to corrections to the sound velocities. These corrections are significant only in the vicinity of the λ point; far away from it, and in particular at very low temperatures, the above approximation is well justified.

First sound in superfluid helium corresponds to ordinary pressure-density waves which is similar to sound in classical fluids. However, the two-fluid nature of superfluid helium introduces modifications to its propagation. Nonlinear effects in first sound become significant at high amplitudes, leading to phenomena such as shock wave formation and harmonic generation. These nonlinearities arise from the dependence of sound velocity on pressure and temperature, as well as interactions between the normal and superfluid components.

5.5.2 Second sound

For perturbations characterized by vanishing total mass–density fluctuation, $\varrho' = 0$, but a finite entropy fluctuation, $S' \neq 0$, helium II supports temperature (second-sound) waves described by Eq.5.58, which propagate with velocity $v = v_2$. In this situation Eq.5.24 implies that the pressure gradient vanishes, $\operatorname{grad} p = 0$. Combining this condition with the Eq.5.8 one obtains

$$\frac{\partial}{\partial t}\left(\varrho_n v_n\right) + \frac{\partial}{\partial t}\left(\varrho_s v_s\right) = 0, \tag{5.61}$$

so that the total momentum density

$$j = \varrho_n v_n + \varrho_s v_s \tag{5.62}$$

is either constant or zero. Since a stationary mass flow cannot be sustained in a closed container, the physically relevant case is $j = 0$, i.e.

$$\varrho_n v_n + \varrho_s v_s = 0. \tag{5.63}$$

Thus the normal and superfluid components move in phase opposition: the two fluids counterflow in such a way that the net mass current vanishes, while a finite entropy (heat) current is transported.

The propagation velocity of these temperature waves (second sound) in helium II is given by

$$v_2^2 = \frac{\varrho_s}{\varrho_n} S^2 \left(\frac{\partial T}{\partial S}\right)_{\varrho} = \frac{\varrho_s}{\varrho_n} \frac{T S^2}{C_p}, \tag{5.64}$$

where S is the entropy per unit mass and C_p is the specific heat at constant pressure. Within Landau's model of helium II, the only relevant excitations at very low temperatures are phonons. Using the phonon expressions for S, C_p, and ϱ_n, one finds in the limit $T \to 0$ that $v_2 \approx \frac{v_1}{\sqrt{3}} \approx 137\ \mathrm{m\,s^{-1}}$, where v_1 is the velocity of first sound.

The velocity of second sound is given by

$$v_2^2 = \frac{\varrho_s}{\varrho_n} S^2 \left(\frac{\partial T}{\partial S}\right)_\varrho , \tag{5.65}$$

which can equivalently be expressed in terms of the specific heat at constant pressure as

$$v_2^2 \approx \frac{\varrho_s}{\varrho_n} \frac{TS^2}{C_p}, \tag{5.66}$$

using $C_p = T(\partial S/\partial T)_p$ for an almost incompressible liquid.

Beyond the linear regime, second sound in helium II displays a rich variety of nonlinear phenomena. At higher excitation amplitudes, second sound waves undergo wave steepening and shock formation, and their velocity becomes amplitude dependent. Experiments have shown that energy injected at a driving frequency is transferred via cascade processes into higher harmonics and eventually dissipated by viscous mechanisms at shorter wavelengths [87]. In addition, nonlinear coupling between first and second sound has been observed: parametric excitation of second sound by first sound leads to three-wave interaction effects such as phase conjugation and giant amplification of the second-sound intensity [88]. Taken together, these results demonstrate that second sound not only serves as a probe of two-fluid hydrodynamics in the linear response regime, but also provides a powerful playground for exploring nonlinear wave dynamics and turbulence in quantum fluids.

5.5.3 Third sound

Third sound is a surface mode propagating in thin superfluid ^{4}He films, characterized by oscillations of the film thickness driven by the motion of the superfluid component, while the normal component remains effectively clamped to the substrate by viscosity [30]. In contrast to bulk sound modes, the mass transport in third sound is dominated by the superfluid fraction alone, since the entropy-carrying normal fluid cannot follow the motion on experimental time scales. In this mode, the superfluid component oscillates parallel to the film surface, and the associated redistribution of superfluid mass leads to periodic variations of the local film thickness. The normal component remains essentially stationary due to its strong viscous coupling to the substrate, so that the restoring forces that drive the disturbance back toward equilibrium act only on the moving superfluid film. The third sound thus represents a surface wave supported by the mobility of the superfluid fraction alone.

In the long-wavelength, small-amplitude limit, the dynamics of third sound can be described, to a good approximation, by the continuity and Euler equations for the superfluid component, supplemented by appropriate boundary conditions at the free surface and at the substrate. Microscopically, the restoring forces governing third-sound dynamics are mainly provided by van der Waals interactions between the helium film and the substrate, by surface tension at the free surface, and by gravity acting on the liquid helium, whereas dissipation due to the clamped normal component and vortex nucleation can be modeled as additional friction terms beyond this ideal hydrodynamic description. The existence of third sound was first confirmed experimentally by measuring the wave velocity and attenuation as functions of film thickness and temperature, which provided key information on film stability and on the superfluid density near surfaces [89].

Because in our experiments we will be dealing with the third sound waves, i.e. superfluid surfaces waves in a thin film, we now described this in detail.

We consider a superfluid ^{4}He film of equilibrium thickness d_0 adsorbed on a rigid substrate. The liquid is treated as incompressible, so that the mass density ϱ can be taken as constant throughout the film. The film is sufficiently thin that the wavelength of third-sound waves satisfies $\lambda \gg d_0$, and the superfluid velocity field $\boldsymbol{v}(\boldsymbol{r}, t)$ is confined to the plane of the film. The normal component is strongly damped by viscous friction with the substrate and is taken to be clamped, so that only the superfluid component participates in the motion.

The restoring force arises from the van der Waals interaction between the helium film and the substrate, which can be represented by a thickness-dependent potential per unit mass,

$$U(d) = \frac{\alpha_{\mathrm{vdW}}}{d^3}, \tag{5.67}$$

where α_{vdW} is the material-dependent van der Waals coefficient. The corresponding acceleration (force per unit mass) in the direction of the film thickness is obtained by differentiating $U(d)$ with respect to d,

$$g_{\mathrm{vdW}}(d) = -\frac{\mathrm{d}U}{\mathrm{d}d} = -\alpha_{\mathrm{vdW}} \frac{\mathrm{d}}{\mathrm{d}d}\left(d^{-3}\right) = 3\,\frac{\alpha_{\mathrm{vdW}}}{d^4}. \tag{5.68}$$

In the two–fluid description the total mass density $\varrho = \varrho_s + \varrho_n$ obeys the continuity equation ($\frac{\partial \varrho}{\partial t} + \mathrm{div}\big(\varrho_s \boldsymbol{v}_s + \varrho_n \boldsymbol{v}_n\big) = 0$), where $\boldsymbol{v}_s$ and $\boldsymbol{v}_n$ denote the superfluid and normal velocities, respectively. For a thin adsorbed film supporting third–sound oscillations, the normal component is clamped to the substrate so that $\boldsymbol{v}_n \simeq \mathbf{0}$. so the mass conservation law can be written as,

$$\frac{\partial \varrho}{\partial t} + \operatorname{div}\big(\varrho_s \, \boldsymbol{v}_s\big) = 0, \tag{5.69}$$

Consider a substrate with area A, the helium film above it forms a column of height d, and its mass is obtained by integrating the mass density over the volume $m = \int_0^d \varrho \, A \, \mathrm{d}z$, dividing by the area A gives the mass per unit area of the film σ,

$$\sigma = \frac{m}{A} = \int_0^d \varrho \, \mathrm{d}z \simeq \varrho d, \tag{5.70}$$

so that local thickness variations directly correspond to variations of the mass per unit area. Thus, the in–plane mass current can be given by $\boldsymbol{j} = \varrho \, d \, \boldsymbol{v}$.

Under the approximation that there is no net mass flux through the substrate or the free surface, we obtain the mass conservation law per of unit area,

$$\varrho \, \frac{\partial d}{\partial t} + \operatorname{div}\big(\varrho_s d \, \boldsymbol{v}_s\big) = 0. \tag{5.71}$$

Considering small-amplitude thickness oscillations of the film and write the local thickness as $d = d_0 + \delta d$, with $|\delta d| \ll d_0$, where δd describes the thickness variations. We obtain

$$\varrho \, \frac{\partial \delta d}{\partial t} + \varrho_s d_0 \, \operatorname{div} \boldsymbol{v}_s + \varrho_s \, \operatorname{div}\big(\delta d \, \boldsymbol{v}_s\big) = 0. \tag{5.72}$$

In the linear approximation we neglect the term $\operatorname{div}(\delta d \, \boldsymbol{v}_s)$, which is of second order in the small quantities δd and $\boldsymbol{v}_s$, we obtain

$$\frac{\partial \delta d}{\partial t} = -\frac{\varrho_s}{\varrho} \, d_0 \, \operatorname{div} \boldsymbol{v}_s. \tag{5.73}$$

Starting from the two–fluid equation Eq.5.16 ($\frac{\partial \mathbf{v}_s}{\partial t} = S \operatorname{grad} T - \frac{1}{\varrho} \operatorname{grad} p$) for the superfluid component acceleration, neglecting temperature gradients ($\operatorname{grad} T \approx 0$, consider the cooling power from the substrates is strong enough to keep the temperature variation tiny), the equation can be written as

$$\frac{\partial \boldsymbol{v}_s}{\partial t} = -\frac{1}{\varrho} \, \operatorname{grad} p, \tag{5.74}$$

In the thin–film geometry considered here, pressure variations are caused by local changes in the film thickness through the van der Waals potential at the substrate.

To linear order, we write $p = \varrho\, g_{\text{vdW}}\, \delta d$. Thus last equation is

$$\frac{\partial \boldsymbol{v}_s}{\partial t} = -\frac{1}{\varrho}\ \mathrm{grad}\big(\varrho\, g_{\text{vdW}} \delta d\big) = -g_{\text{vdW}}\ \mathrm{grad}\, \delta d. \tag{5.75}$$

Taking the time derivative of Eq. 5.73 and using Eq. 5.75, we obtain

$$\begin{aligned}\frac{\partial^2 \delta d}{\partial t^2} &= -\frac{\varrho_s}{\varrho}\, d_0\, \frac{\partial}{\partial t}\big(\mathrm{div}\, \boldsymbol{v}_s\big) = -\frac{\varrho_s}{\varrho}\, d_0\ \mathrm{div}\left(\frac{\partial \boldsymbol{v}_s}{\partial t}\right)\\ &= -\frac{\varrho_s}{\varrho}\, d_0\ \mathrm{div}\left(-g_{\text{vdW}}\ \mathrm{grad}\, \delta d\right) = d_0\, \frac{\varrho_s}{\varrho}\, g_{\text{vdW}}\ \mathrm{div}\big(\mathrm{grad}\, \delta d\big).\end{aligned} \tag{5.76}$$

This is a wave equation of the form

$$\frac{\partial^2 \delta d}{\partial t^2} = c_3^2\, \nabla^2 \delta d, \qquad c_3^2 = \frac{\varrho_s}{\varrho}\, d_0\, g_{\text{vdW}} = 3\, \frac{\varrho_s}{\varrho}\, \frac{\alpha_{\text{vdW}}}{d_0^3}, \tag{5.77}$$

where c_3 is the third-sound velocity and can be written as

$$c_3 = \sqrt{3\, \frac{\varrho_s}{\varrho}\, \frac{\alpha_{\text{vdW}}}{d_0^3}}. \tag{5.78}$$

The third–sound velocity increases when the substrate–induced van der Waals attraction becomes stronger, and that scales as $c_3 \propto d_0^{-3/2}$ so that thinner films support faster propagation. At fixed substrate and film thickness, c_3 is further reduced when the superfluid density ϱ_s becomes smaller, for example as the temperature approaches the lambda transition.

The superfluid density ϱ_s is an equilibrium property of the film. It is set by the thermodynamic state (in particular the temperature and the spectrum of excitations) and may vary between different experimental conditions. In the third–sound geometry considered in this thesis we focus on isothermal perturbations with $\delta T \approx 0$ and small relative thickness variations $\delta d \ll d_0$ about a homogeneous equilibrium film. Within this linear approximation the wave does not appreciably modify ϱ_s, and in Eq. (5.78) it should be understood as the equilibrium value $\varrho_s(T_0)$ appropriate to the chosen temperature.

Possible corrections due to finite temperature variations and evaporation–condensation processes, as illustrated in Figure 5.3, can be added in the form of

$$c_3 \approx \sqrt{3\, \frac{\varrho_s}{\varrho}\, \frac{\alpha_{\text{vdW}}}{d_0^3}(1 + \frac{T\, S}{L})}, \tag{5.79}$$

where L denotes the latent heat of vaporization. At T_λ, this additional correction is about 0.15 and decreases to 0.1 at 1 K [30]. In our experiments, we expect that the third-sound wave velocity is barely influenced by this correction term because the base temperature is on the order of 20 mK.

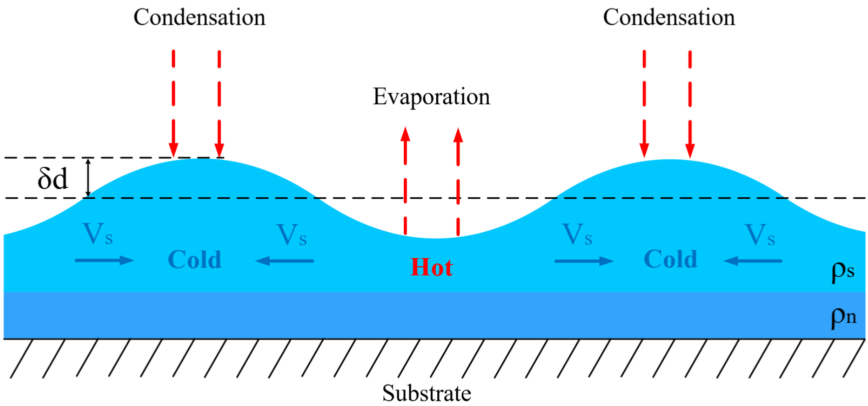

Figure 5.3: The third sound waves is a surface wave of the superfluid component of the superfluid Helium. The restoring force is the van der Waals force with the substrate. The normal component resides at the interface with the substrate due to its non-zero viscosity, and does otherwise not participate in the third sound dynamics. The red errors indicate the process of partial evaporation and condensation of the superfluid component, which can give rise to a modification of the third sound velocity. The maximum correction can be 15% when the system operates close to the Lambda point. Adapted from [90].

Within the two-fluid description, first, second, and third sound appear as different collective modes of the same superfluid: one dominated by density oscillations, one by entropy flow, and one by thickness variations in a film. These modes can be interpreted as macroscopic manifestations of the excitation spectrum, with their velocities and damping governed by the quasiparticles and their interaction with the superfluid background. In the next section we analyze the excitation spectrum and discuss how it limits the maximum superflow velocity.

5

5.5.4 Landau criterion and vortices

In bulk, the system supports phonon excitations at low momentum and roton excitations at intermediate momenta, and the resulting energy–momentum dispersion relation determines the critical velocity below which superfluid flow remains dissipationless. The same quasiparticle spectrum constrains the stability of superfluid flow in thin films: as long as the characteristic flow velocities associated with third-sound oscillations remain below the Landau critical velocity, the mode propagates with very low dissipation, whereas at higher amplitudes the creation of quasiparticle excitations provides a microscopic mechanism for damping and eventual breakdown of superfluidity in the film.

Landau's theory further complements the two-fluid model by introducing a quasiparticle description of excitations in helium II [28]. In the Landau picture, this threshold is the critical velocity v_c at which the creation of elementary excitations becomes energetically allowed. It is determined by the excitation spectrum $\varepsilon(p)$ of the superfluid via

$$v_c = \min_p \frac{\varepsilon(p)}{p}. \tag{5.80}$$

As long as the flow velocity v is below v_c, energy and momentum conservation forbid the spontaneous creation of phonons, rotons, or vortices, and the flow remains dissipationless. This criterion applies not only to uniform bulk flow, but also constrains the stability of hydrodynamic modes such as first sound, second sound, and surface excitations in thin films: as long as the characteristic flow velocities associated with these modes remain well below v_c, their damping due to quasiparticle production is strongly suppressed.

Once v exceeds v_c, excitations can be created and thereby lead to dissipation and a breakdown of superfluidity.

In a simply connected region the superfluid velocity field is irrotational, but in multiconnected geometries circulating flow can be supported by vortex lines or vortex rings whose circulation is quantized in units of $\kappa = h/m_4$. When the flow velocity relative to boundaries or obstacles becomes sufficiently large, it may become energetically favorable to create vortices, which provides an efficient channel for converting ordered superflow into excitations and heat. In practice, the onset of dissipation in superfluid helium flows is frequently governed by vortex nucleation rather than by the ideal Landau critical velocity, and the same consideration applies to high-amplitude third-sound oscillations in thin films, where vortex-mediated damping sets a practical limit to the stability of the mode.

Quantized vortices in superfluid helium-4 are a direct manifestation of macroscopic quantum coherence, arising from the topological constraint that the macroscopic wavefunction must remain single-valued. These vortices constitute topological defects with quantized circulation, reflecting the requirement that the phase of the superfluid order parameter returns to itself modulo 2π around any closed path. Since the superfluid velocity is proportional to the gradient of this phase, the circulation is quantized in discrete units of $\hbar/m_4$, where $m_4$is the mass of a helium-4 atom.

The concept of quantized circulation was first introduced by Lars Onsager [91] in 1949 and further developed by Richard Feynman [92], who postulated that superfluid helium, when set into rotation, does not exhibit rigid-body motion but instead forms a lattice of quantized vortices to conserve angular momentum. In such a vortex, the superfluid density vanishes at the core, and the surrounding flow exhibits a $1/r$ velocity profile.

Experimental validation of quantized vortices began with the work of George W. Rayfield and Frederick Reif [72], who generated charge-carrying vortex rings in superfluid helium and analyzed their interactions with phonons, rotons, and impurities. These experiments not only confirmed the existence of quantized vortices but also provided estimates of the vortex core radius, found to be on the order of 1 Ångström. Subsequent studies by Gamota [93] demonstrated the generation of vortex rings by forcing superfluid through orifices above a critical velocity. More recent visualization techniques, such as nanoparticle tracking methods developed by Minowa et al., have enabled direct observation of vortex lines, their reconnections, and Kelvin wave excitations.

Quantized vortices in superfluid helium-4 are not static. They can interact, reconnect, and form complex tangles, leading to a state known as quantum turbulence. Unlike classical turbulence, which involves a continuous vorticity field, quantum turbulence is composed of discrete vortex filaments. Reconnection events and the subsequent excitation of Kelvin waves enable energy to cascade to smaller length scales, eventually dissipating via phonon emission, even in the absence of viscosity.

In the bulk (3D) system, vortices are extended line-like defects capable of forming entangled networks and supporting Kelvin waves. In contrast, in thin films (2D), vortices manifest as point-like singularities and are often studied within the framework of the Berezinskii–Kosterlitz–Thouless (BKT) transition, where vortex–antivortex pairs unbind at a critical temperature, driving a transition from superfluid to normal behavior [94]. The confinement to two dimensions alters both the energetics and dynamics of vortex interactions, and thus thin-film systems serve as valuable platforms for probing low-dimensional quantum fluid phenomena.

In summary, quantized vortices not only serve as fundamental signatures of the superfluid state but also provide a crucial link between microscopic quantum behavior and macroscopic fluid dynamics. Their study continues to deepen our understanding of rotational responses, turbulence, and non-equilibrium quantum phenomena in superfluid helium.

5.6 A simple model of chaos: logistic map

One of the simplest illuminating models for understanding the onset of chaos in nonlinear dynamical systems is the logistic map. This model, originally introduced by Robert May in the 1970s within the context of population biology, was formulated to capture how the population of a group evolves over time under limited resources. It assumes that the growth of a population is not only proportional to its current size but is also inhibited by competition and environmental constraints. Mathematically, the model takes the form of a one dimensional discrete-time recurrence relation:

$$x_{n+1} = rx_n(1 - x_n), \tag{5.81}$$

where x_n represents the normalized population at the n-th iteration ($0 \leq x_n \leq 1$) and r is a dimensionless control parameter representing the population's intrinsic growth rate. Despite the simplicity of its formulation, this map exhibits remarkably rich dynamical behavior as the parameter r is varied.

At small values of r, the system stabilizes to a fixed point, corresponding to a stable equilibrium population. As r increases beyond the critical threshold, this fixed point becomes unstable and the system starts to experience the period-doubling bifurcations. The period of oscillations doubles successively, giving period-2, period-4, period-8, and eventually period of 2^n. The bifurcation intervals become smaller in a geometric way and reach a limit at a critical value at $r \approx 3.57$. Beyond this point, the system becomes chaotic, showing behavior that is aperiodic, bounded, and highly sensitive to initial conditions.

5

This standard route to chaos, known as the Feigenbaum scenario [95, 96], has been widely identified across disciplines including fluid dynamics, electronic circuits, chemical oscillations, and astrophysical systems. Its characteristic period-doubling bifurcations have also been observed experimentally in diverse platforms such as fluid convection, lasers [97], Josephson junctions, plasma instabilities, and chemical reactions [16].

In the quantum optics and optomechanical systems, these bifurcations frequently mark the transition from regular to chaotic motion. Similar behavior has been observed in our studies of superfluid helium thin films, where nonlinear interactions between excitations give rise to complex temporal dynamics. These findings emphasize that such dynamical phenomena are not only mathematical abstractions, but rather universal features of nonlinear systems.

The ubiquity of the period-doubling route to chaos reinforces the logistic map as a minimal yet powerful model for capturing the essential features of complexity in deterministic settings. It not only provides a simple framework for illustrating the transition from regular to chaotic behavior but also offers meaningful insights into real-world nonlinear dynamics. Its bifurcation diagram visually reveals distinct dynamical regimes as the control parameter is varied.

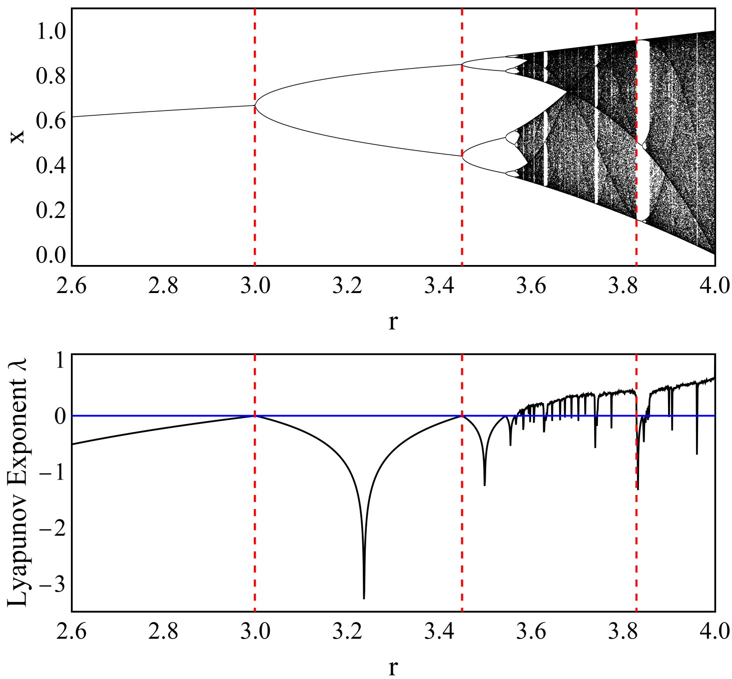

Figure 5.4: Bifurcation diagram (top) and Lyapunov exponent (bottom) of the logistic map for $r \in [2.6, 4.0]$. Red dashed lines indicate the transition points, including the beginning of bifurcation near $r = 3.0$, period-doubling accumulation ($r \approx 3.45$), the onset of chaos ($r \approx 3.57$), and a periodic window within the chaotic regime ($r \approx 3.83$). The blue horizontal line marks the zero Lyapunov exponent, separating stable ($\lambda < 0$) and chaotic ($\lambda < 0$)regions.

To visualize these dynamical transitions, Figure 5.4 presents the bifurcation diagram of the logistic map (top figure), accompanied by a plot of the associated Lyapunov exponent $\lambda(r)$, both plotted as functions of the control parameter $r \in [2.6, 4.0]$. The bifurcation diagram is constructed by iterating the map over a large number of steps, discarding transients, and plotting the steady-state values of x_n. As r increases from left to right, one observes the transition from a fixed point to periodic orbits, followed by a rapid succession of bifurcations, eventually giving rise to a densely populated chaotic regime. Embedded within the chaotic regions are windows of periodicity where the system temporarily regains regular behavior before bifurcating again. These periodic windows, often of periods three, five, or higher, serve as a visual manifestation of the intricate structure of chaotic attractors.

The Lyapunov exponent provides a quantitative measure of the system's sensitivity to initial conditions and is defined by the time averaged logarithmic divergence of infinitesimally close trajectories. For the logistic map, it takes the form:

$$\lambda(r) = \lim_{n\to\infty} \frac{1}{n} \sum_{i=1}^{n} \log |f'(x_i), | \tag{5.82}$$

where $f(x) = rx(1-x)$. When $\lambda < 0$, nearby trajectories converge and the system exhibits stable oscillation. When $\lambda = 0$, the system is at the verge of bifurcation. When $\lambda > 0$, infinitesimal differences grow exponentially with time, signaling the onset of deterministic chaos. As illustrated in the lower panel of Figure 5.4, the Lyapunov exponent stays negative when the dynamics remain regular and periodic, approaches zero at bifurcation points, and becomes positive as the system exhibits chaos. Notably, the Lyapunov exponent fluctuates within the chaotic regime, reflecting the intermittent emergence of periodic windows. The horizontal line at $\lambda = 0$ marks the boundary between stable and chaotic behavior, offering a clear diagnostic for distinguishing qualitatively different dynamical regimes.

While the bifurcation diagram and Lyapunov exponent capture the qualitative changes in the system's dynamics, they offer no information about the oscillatory structure of individual trajectories. The vertical axis of the bifurcation diagram shows only a collection of asymptotic values of x_n , without specifying their temporal order or periodicity. To address this limitation, frequency domain analysis provides a natural complement. By applying a discrete Fourier transform (DFT) to the time series x_n, one can extract the spectral composition of the system's dynamics for various values of$r$. This approach reveals how energy is distributed among different frequencies and offers insight into the periodicity, subharmonic structure, and spectral broadening associated with the transition to chaos.

Figure 5.5 shows the amplitude spectra for selected values of r, corresponding to key dynamical transitions highlighted in Figure 5.4. Each spectrum in Figure Figure5.5 is obtained by discarding the initial transient evolution, subtracting the mean to remove the DC component, and computing the magnitude of the DFT for the remaining segment. The resulting spectra are vertically offset to facilitate comparison. At low values such as $r = 3.46$, a single dominant peak appears, signaling stable periodic

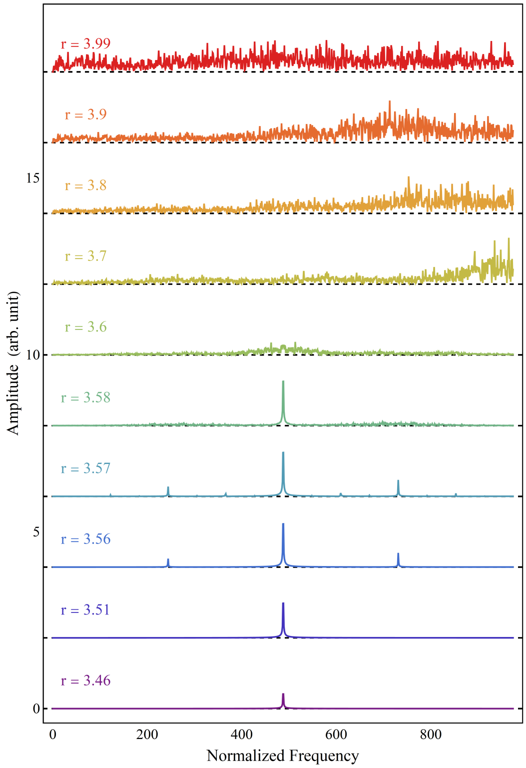

Figure 5.5: Discrete Fourier spectra of the logistic map trajectories for selected values of the control parameter r, showing the progression from periodic dynamics (bottom) to fully developed chaos (top). Each spectra is offset vertically for clarity. As r increases from 3.46 to 3.99, the system transitions from the periodic behavior with a single spectral peak to a broadband chaotic regime with complex spectral structure. The emergence of period doubling peaks and eventual spectral broadening reflect the progression through period-doubling bifurcations and the onset of chaos.

oscillations.

As r increases to 3.51 and 3.56, additional peaks emerge at integer fractions of the base frequency, consistent with the period doubling cascade predicted by Feigenbaum theory in the logistic map dynamics. At $r = 3.57$ and $r = 3.58$, the spectrum becomes increasingly dense, reflecting the beginning of absence of periodicity.

Beyond $r \approx 3.6$, the spectra undergo a qualitative shift: discrete peaks give way to a broadband structure with no dominant frequency components, characteristic of chaotic behavior. For higher value of r, such as $r = 3.9$ and $r = 3.99$, the spectrum resembles that of a broadband noise process, indicating chaotic dynamics and the loss of temporal coherence. The evolution of the spectra captures the gradual loss of frequency coherence, marking the transition to chaos.

Together, the bifurcation structure, Lyapunov exponent, and frequency domain analysis provide a comprehensive and self-consistent picture of the route to chaos in the logistic map. This trifocal perspective not only captures the transitions between dynamical regimes, but also resolves the fine structure of bifurcations and the progressive accumulation of instabilities.

The logistic map illustrates how core features of chaos can emerge from minimal nonlinear rules, such as period-doubling, spectral broadening, and sensitivity to initial conditions. Although simple in form, the spectral features identified here are not unique to the logistic map. The framework developed in this section offers insight into coherence loss and frequency complexity in more complex systems. In the following section, we extend this perspective to an experimental platform: thin superfluid helium films, where strong nonlinear interactions give rise to similar spectral signatures suggestive of chaotic behavior.

5.7 Nonlinear third-sound dynamics with photothermal effects

Third sound in a superfluid helium film is a surface-thickness wave of the superfluid component. Its restoring force is set primarily by the van der Waals interaction between the film and the substrate, so that both the mode frequency and the intrinsic mechanical nonlinearity depend sensitively on the film thickness. In recent work on thin-film superfluid optomechanics [98, 99], this nonlinearity has been traced to the nonlinear thickness dependence of the van der Waals potential, which can give rise to cubic and quartic corrections to the effective mode potential. At the same time, experiments on optically coupled superfluid films have shown that the mechanical response can be strongly modified by radiation pressure and, in particular, by delayed photothermal forces associated with local heating and superfluid flow. In the following, we therefore use a reduced single-mode model that combines these two ingredients. It is not intended as a complete microscopic description of our device, but as a phenomenological framework for discussing the onset of nonlinear dynamics under optical driving.

In our system, the optical field couples to the superfluid helium film through both direct radiation-pressure forces and absorption-induced photothermal effects. The latter can be particularly important in thin superfluid films, where local heating modifies the film dynamics through delayed thermal response and superfluid flow. By contrast, the direct optomechanical coupling is expected to remain comparatively weak, since the spatial overlap between the optical mode and the third-sound motion is limited. For this reason, the model used below places particular emphasis on photothermal backaction, while retaining radiation pressure as an additional optical driving channel.

For a single third-sound mode with generalized coordinate $x(t)$, we write

$$m_{\text{eff}}\ddot{x}(t) + m_{\text{eff}}\Gamma_m\dot{x}(t) + m_{\text{eff}}\omega_m^2 x(t) + \alpha_2 x^2(t) + \alpha_3 x^3(t) = F_{\text{RP}}(t) + F_{\text{PT}}(t). \tag{5.83}$$

Here m_{eff}, ω_m, and Γ_m are the effective mass, resonance frequency, and damping rate of the selected mode. The coefficients α_2 and α_3 represent the lowest-order intrinsic nonlinearities of the mode. In practice, depending on the mode symmetry and operating amplitude, the dominant nonlinear correction may often be approximated by a Duffing-type cubic term.

The intracavity optical field $a(t)$ is described by

$$\dot{a}(t) = -\left[\kappa - i\left(\Delta + gx(t)\right)\right]a(t) + \sqrt{2\kappa_{\text{in}}}\,a_{\text{in}}(t), \tag{5.84}$$

where κ is the optical decay rate, κ_{in} is the input coupling rate, Δ is the laser detuning from the cavity resonance, and g denotes the dispersive optomechanical coupling coefficient.

The optical force is separated into an instantaneous radiation-pressure contribution and a delayed photothermal contribution,

5

$$F_{\text{RP}}(t) = \hbar g\,|a(t)|^2, \tag{5.85}$$

$$F_{\text{PT}}(t) = \hbar g\,\beta A \int_{-\infty}^{t} \frac{du}{\tau_t} e^{-(t-u)/\tau_t} |a(u)|^2. \tag{5.86}$$

The dimensionless factor βA sets the strength and sign of the photothermal response relative to radiation pressure, while τ_t is the characteristic thermal response time.

For numerical convenience, the delayed photothermal term can be rewritten by introducing the memory variable

$$I(t) = \int_{-\infty}^{t} \frac{du}{\tau_t} e^{-(t-u)/\tau_t} |a(u)|^2, \tag{5.87}$$

which obeys

$$\dot{I}(t) = \frac{1}{\tau_t}\left(|a(t)|^2 - I(t)\right). \tag{5.88}$$

The coupled equations then become

$$\dot{x}(t) = \frac{p(t)}{m_{\text{eff}}}, \tag{5.89}$$

$$\dot{p}(t) = -m_{\text{eff}}\omega_m^2 x(t) - \Gamma_m p(t) - \alpha_2 x^2(t) - \alpha_3 x^3(t) + \hbar g|a(t)|^2 + \hbar g\beta A\, I(t), \tag{5.90}$$

$$\dot{a}(t) = -\left[\kappa - i\left(\Delta + gx(t)\right)\right] a(t) + \sqrt{2\kappa_{\text{in}}}\, a_{\text{in}}(t), \tag{5.91}$$

$$\dot{I}(t) = \frac{1}{\tau_t}\left(|a(t)|^2 - I(t)\right). \tag{5.92}$$

In the present thesis, this model is used only as a qualitative framework. It captures the competition between intrinsic third-sound nonlinearity and delayed optically induced backaction, but it does not provide a complete quantitative description of the observed dynamics in our device.

In the next chapter we turn to an experimental realization of a superfluid optomechanical system in which third sound dynamics and the photothermal effect are investigated, resulting in the observation of the strong nonlinear superfluid dynamics.